TECHNISCHE MECHANIK, 30, 1-3, (2010), 227 – 243
submitted: October 31, 2009

Investigation of the grain-scale deformation in a polycrystalline aluminum alloy

T. Marin, G. Nicoletto

A finite element based crystal plasticity implementation is employed to study an aluminum polycrystal subjected to uniaxial loading. The emphasis is put on the effect of the representation of the microstructure on the strain accumulation and intra-granular misorientation field. To better capture the crystal-scale behavior, each grain in the mesh is discretized into many finite elements. It is found that irregular tessellations based on Voronoi schemes provide similar responses whereas regular solids show some differences. An extended investigation of the role of the grain boundaries in the development of strain heterogeneity and in the re-orientation of parts of the grains is also provided according to an original averaging procedure.

1 Introduction

The interaction of grains and the way this influences the performance of a polycrystalline metallic material represent a fascinating stimulus for experimental and numerical research. The anisotropic nature of crystallographic slip determines deformation incompatibilities that are accommodated by local phenomena such as plastic strain heterogeneity, grain reorientation and surface roughening, (Raabe et al., 2003). The distribution of strain that arises in the microstructure is affected by macroscopic factors, such as the load condition, but also by the micro-scale behavior of the grains constituting the polycrystalline aggregate. The topology and the shape of the crystals, the grain boundaries spatial distribution together with the individual lattice orientation are all contributing to the character of the local deformation. The resulting elastic-plastic strain patterns have a scale that spans many grains, but some relevant phenomena, such as grain subdivision and intra-granular misorientation evolution, take place at the scale of the single crystal, (Thorning et al., 2005). In the grains of a polycrystalline material subjected to large plastic deformations, dislocation structures develop with boundaries that might separate volumes with different lattice orientations. This mechanism leads to different rotation paths and rates and to deformation induced grain boundaries with a certain misorientation between the domains, (Hughes and Hansen, 1997; Kuhlmann-Wilsdorf and Hansen, 1991). At least three factors promote this behavior: plastic anisotropy, the highly non linear relation between stress and shear strain rate that controls crystallographic slip, and the constraining effect due to the neighboring grains. The deformation induced is heterogeneous and often characterized by localized regions of highly strained material surrounding portions that have undergone less deformation, or by the splitting of the grain in two or more areas rather homogeneously deformed according to different slip systems. Somehow the localization of straining is lessened by work hardening that tends to spread the deformation over wider areas. Full-field measurements methods, such as digital image correlation, can be used to investigate the evolution of deformation on the surface of the specimens and often reveal a direct connection of the strain patterns to the underlying microstructure, (Tatschl and Kolednik, 2003). Moreover techniques such as orientation imaging microscopy and X-ray microdiffraction can provide detailed information regarding the local grain orientation in highly resolved areas, (Kamaya et al., 2005). In addition to experimental tools, finite element simulations of polycrystals can be used to analyze deformation and re-orientation phenomena at the grain scale and monitor microstructural features related to lattice orientation, (Kalidindi et al., 2004). While experimental data are available only at limited load levels and at specific locations in the sample, with the FE calculations a wide range of information is accessible through the whole deformation history and in all the elements of the model. In this work numerical simulations are employed to study some aspects of strain distribution and of intragranular lattice misorientations in an aluminum alloy. The goal, is to better understand quantitative trends related to the role of the grain boundaries, and to asses how the representation of the microstructural features such as the grain shape and arrangement, affects the response of the polycrystal both at the macroscale and at the crystal-level scale.

2 Micromechanical modeling of polycrystalline materials

The simulations presented are based on the finite element method; within this context four main issues are involved in the modeling of polycrystalline materials:

1. the choice of the scale
2. the definition of constitutive equations
3. the construction of an appropriate microstructure representative of the material
4. the application of suitable boundary conditions.

The phenomena analyzed in the following sections regards the local behavior of the crystals in an aluminum alloy, therefore the way the grains behave and interact must be included in the modeling effort. The finite element formulation employed is three-dimensional, allowing a complete definition of the spatial domain, and is based on an elasto-viscoplastic constitutive model that describes the behavior of the material at the crystal scale. The elastic response is linear and anisotropic while the rate-dependent plastic response is cast in terms of crystallographic slip. In a material with FCC crystal structure, crystallographic glide is assumed to take place on twelve $\{111\} < 110>$ slip systems, being $\{111\}$ the planes of greatest atomic density and $<110>$ the close-packed directions within those planes. To better detect the grain interaction and the intra-granular heterogeneities that develop upon deformation, no mean field assumptions (such as Taylor hypothesis) are used to relate the single crystal to macroscopic polycrystal response. Instead each grain is discretized into a number of finite elements and the constitutive equations are enforced at the quadrature points without homogenization. An insight into the model and its implementation is yielded in Section 4.

In FE crystal plasticity simulations, artificial (or virtual) polycrystals constituted by aggregate of grains have to be constructed and the level of details adopted in representing the microstructure depends on the phenomena object of the study. For example texture analysis at large deformation can be dealt with cubic grains, (Sarma and Dawson, 1996), while for the study of strain heterogeneities more realistic grain shape have to be used, (Zhang et al., 2005). Until few years ago, micrographs of physical microstructures were usually the most common source of information to infer the spatial distribution of phases, grain morphology and topology. Orientation mapping have then emerged as a powerful metallographic technique for characterizing grain structures; nevertheless both methods are two-dimensional in nature. A full three-dimensional description is possible through serial slicing, (Sumigawa et al., 2004), or sophisticated nondestructive techniques based on diffraction, (Fu et al., 2003). The modeling of real microstructures is necessary when experimental data, extracted in a well defined portion of the material, is directly compared to simulation results. This has been done almost exclusively through full-field measurements of displacements or orientations on the surface of specimens to correlate strain patterns to grain boundaries or to investigate deformation bands, see for example (Sachtleber et al., 2002; Erieau and Rey, 2004; Héripré et al., 2007). The procedure for the assembly of the grain aggregates used in this work is expanded in Section 3.

The fourth point concerns the way the virtual polycrystals are constrained and loaded. In this study an aluminum alloy subjected to monotonic uniaxial loading is considered ant the maximum engineering strain reached is 10%. Details on the boundary conditions and on the application of the deformation history to the finite element meshes are provided in Section 5.

3 Virtual grain aggregates for FE modeling

When introducing the methodology in Section 2, it was recalled that the reconstruction of grain aggregates from experimental evidence may not be straightforward and not always necessary. The easier and more viable way consists in the arrangement of artificial polycrystalline aggregates, and this has also been the most widely used procedure in the literature. Another undoubted advantage is that different microstructures can be analyzed and compared and hints about the role of the grain geometry and arrangement might be drawn. The present work in fact targets at contributing to the understanding of the implications of some modeling choices on the intra-granular response of the FCC materials. The definition of an aggregate of non-overlapping and space-filling grains poses many questions about shape and spatial distribution of the constituent grains. For example the grains could be regular or irregular solids, convex or concave. In the literature convex shapes have been utilized almost exclusively due to their simpler construction; concave grains are not considered here.

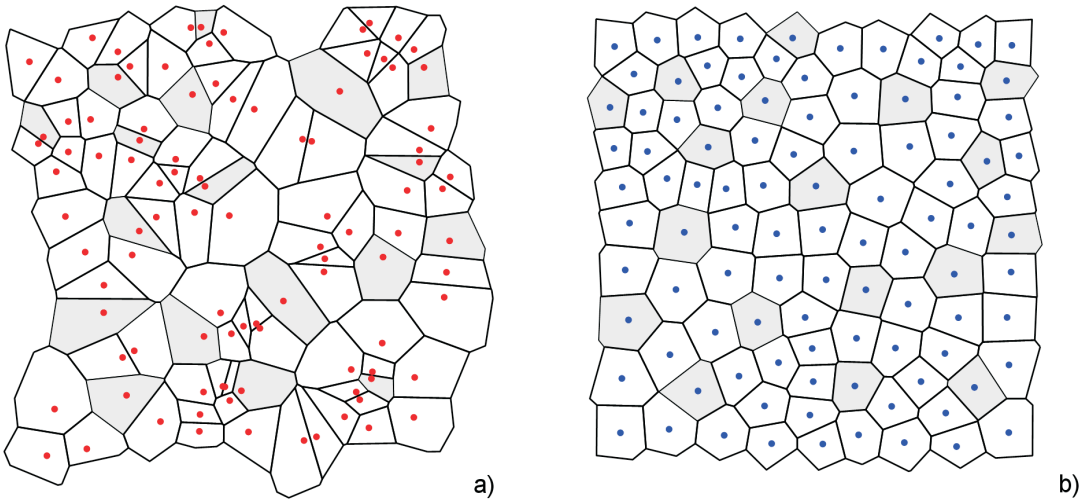

Figure 1: (a) 2D Voronoi tessellation generated by 100 randomly distributed nucleation points (indicated by the marks), and (b) the corresponding centroidal Voronoi tessellation. The aggregate has periodic boundaries.

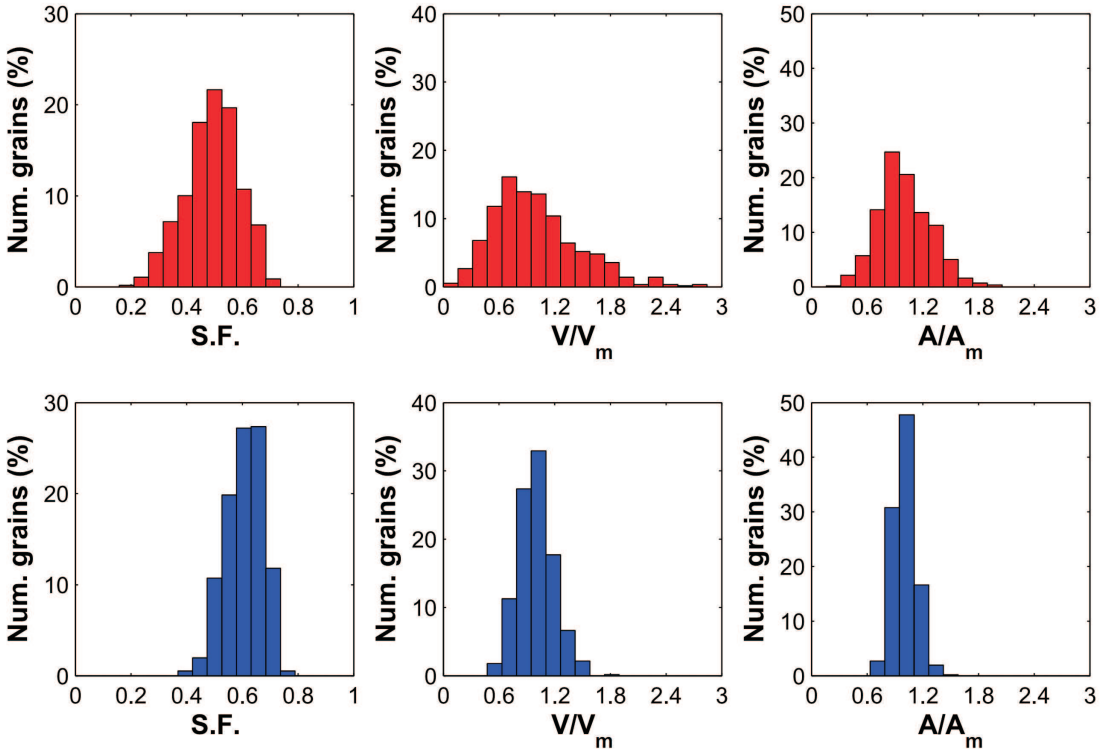

Figure 2: Distributions of the shape factor (SF), normalized volume (V/V_m) and normalized area (A/A_m) in the 559-grain 3D polycrystals *VOR3* (top row) and *CVT3* (bottom row).

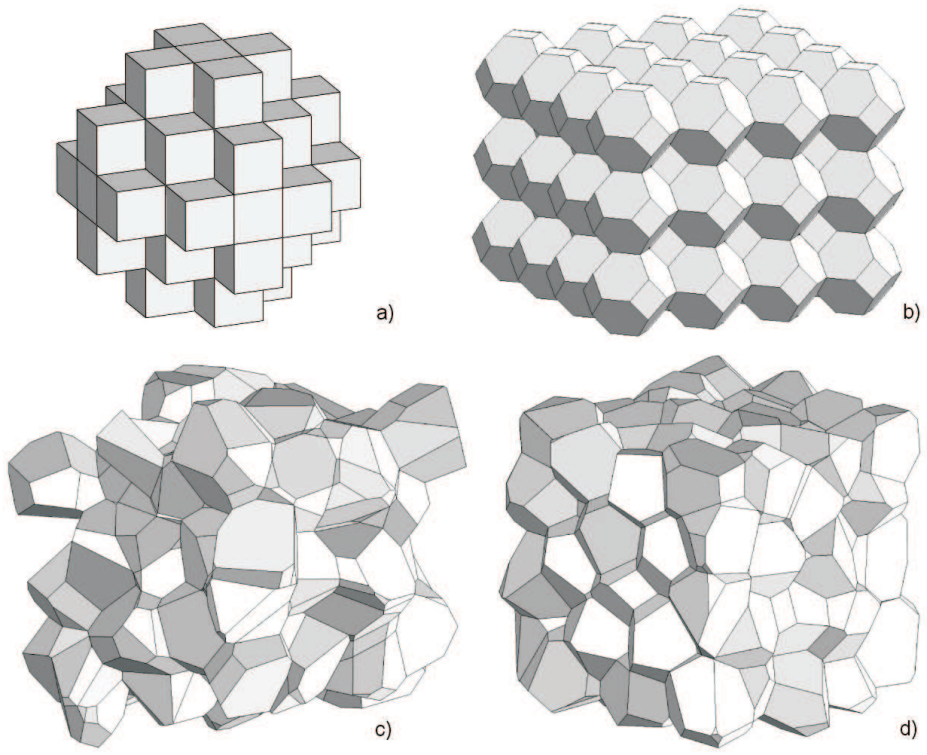

Figure 3: Tessellation of space using (a) cubes, (b) truncated octahedra, (c) Voronoi cells and (d) centroidal Voronoi cells obtained from (c).

The approach that uses regular solids tiled periodically does not require special efforts. There are many space-filling convex polyhedra with regular faces, (e.g. tetrahedron, triangular prism, gyrobifastigium, ...) but only five of them can be tiled keeping the same orientation in space: cube, hexagonal prism, elongated dodecahedron, truncated octahedron and rhombic dodecahedron. There exist other space-filling solids that do not keep the orientation or that do not have regular faces. Different shapes can be combined together to obtain a tessellation but this practice is not common in polycrystals modeling. Cube is the simplest geometry, the tiling is trivial and the realization of regular mesh, using brick or tetrahedral elements, is straightforward. These are the reasons for their extensive use in the past, for example (Dawson et al., 2001). The disadvantage of this solid is that the shape is quite far from real grains, furthermore the faces are aligned in a "grid" and the number of neighbors is constant and fixed to only six. To overcome those drawbacks but preserving the "meshability", rhombic dodecahedron and truncated octahedron are good candidates. The first one has 12 faces, 24 edges and 14 vertices; every face has 4 edges. The truncated octahedron has 14 faces (6 squares and 8 hexagons), 24 vertices and 36 edges; it is characterized by the property that 3 edges meet at every vertex and that, in a periodic pattern, every edge is shared by just 3 adjacent solids. The cube ant the truncated octahedron can be inscribed in a sphere while the rhombic dodecahedron cannot. Incidentally, it is known from basic crystallography that the Wigner-Seitz cell of simple cubic lattice unit cell (SC) is the cube, for the body-centered cubic lattice (BCC) it is the truncated octahedron and finally for the face-centered cubic lattice (FCC) it is the rhombic dodecahedron. The shape factor, defined for a three-dimensional body in Equation 1, is an effective means for the characterization of the geometric shapes:

$$SF = \frac{36\pi \cdot V^2}{A^3} \tag{1}$$

where V is the volume and A is the surface area of the solid. It is a dimensionless parameter ($0 \leq SF \leq 1$) that becomes unity for spherical bodies and decreases in value with increasing shape irregularity. It results that: cube $SF = 0.52$, rhombic dodecahedron $SF = 0.74$ and truncated octahedron $SF = 0.75$.

Another common method for the construction of aggregates of solids is the Voronoi tessellation. It has been widely adopted as a modeling tool in many fields in materials science such as the simulation of grain growth, crack growth, damage and shear banding in polycrystals. The applications of Voronoi tessellation are however not restricted to mechanical problems. Among others, simulation of magnetisation processes, study of foams, and

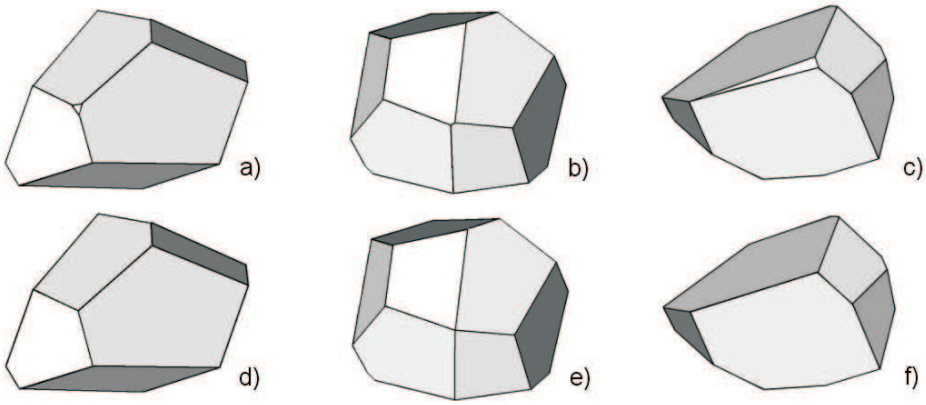

Figure 4: Examples of grains with geometric features that affect the size and the quality of the mesh: (a) small faces, (b) small edges and (c) small angles. (d-f) Removal of the small features.

concrete. The Voronoi algorithm is renowned for being able to create stochastic microstructures that well resemble typical grain aggregates. In short, a *n*-dimensional space is partitioned into convex and space-filling polytopes: in 2D this results in polygons, whereas in 3D the outcome is a cell structure of polyhedra with planar faces that are the perpendicular bisectors of the segments joining the nucleation point with the other neighbors. The subdivision of the space is completely determined by the position of the set of nucleation points (or seeds). The Voronoi tessellation mimics the morphogenetic process of nucleation and radial growth from fixed seeds in a isotropic and homogeneous way. The cells have the interesting feature that all the vertices act as "triple junctions": exactly three cells meet at every corner. It follows that each edge is in contact with just 3 polyhedra in 3D (2 polygons in 2D). This characteristic is shared by cubic shapes and by truncated octahedra but not by rhombic dodecahedra. Since the discrete set of nucleation points completely defines the resulting cell structure, it might be envisaged that one could position them in such a way to create certain types of polyhedra with a specific stereology, but in general this is not straightforward. A random set of points is most often used and a very complex cell structure is then produced. Two issues arise, the first is related to the "meshability" of the grains: the more complex is the geometry of the grains, the higher is the number of finite elements required. The second concerns the accuracy in the representation of the microstructure in terms of grain size distribution. If a particular distribution is found in the material studied and if this is considered relevant for the modeling then the nucleation points have to be placed with *ad hoc* procedures.

A special type of Voronoi tessellation, called centroidal Voronoi tessellation, has the distinct property that ideally the nucleation points coincide with the centroids of the cells. This has an impact on the size and shape distributions of the grains, simply speaking the seeds get well-spaced and the size distribution is less spread. Several algorithms can be used to generate this special tessellation, for instance it can be obtained from a pre-existing Voronoi tessellation through an iterative minimization process of the distance between the centroid and the nucleation point in all the cells. Figure 1 shows an example of tessellation of a portion of a plane by 100 cells, the external bounds are also shaped to allow a periodic tiling of the whole aggregate: on the left the Voronoi tessellation generated by random seeds, on the right the corresponding centroidal Voronoi tessellation. Some cells are highlighted to better track their evolution. It is evident how the minimization process heavily alters the position and geometry of the cells and how a higher degree of uniformity in shape and size is gained. To create such aggregates, some Matlab scripts based on the routines by prof. J. Burkardt [1] were implemented by the authors. A detailed investigation of the theory of the centroidal Voronoi tessellation and of the mathematical aspects may be found in (Du et al., 1999). Figure 2 shows an example of grain statistics in a Voronoi tessellation and in the related centroidal Voronoi tessellation for a cube filled with 559 nucleation points randomly distributed (these aggregates will be called *VOR3* and *CVT3* in the subsequent parts of the paper). Three parameters are plotted in form of histograms: the shape factors SF, the grain volumes V normalized by the mean value V_m, and the area A of the grain surfaces normalized by the mean value A_m. The mean shape factor for *VOR3* is 0.49 while for *CVT3* it is 0.61 which is about 25% higher, so the grains in *CVT3* are somehow more spheroidal. Aggregate *VOR3* has a mean shape factor quite low and comparable to the cubic grains; it is also fairly far from both rhombic dodecahedra and truncated octahedra, these regular solids are not even reached by the grains in *CVT3*. In the centroidal Voronoi tessellation not only the grains are more equiaxed but also the size dispersion is reduced as can be seen inspecting the scatters in the histograms of the top and bottom rows of Figure 2. The normalized volume V/V_m and area A/A_m tend to concentrate more in proximity of 1, which stands for the case of iso-volume and iso-area, but some scatter is still present. The absence

[1] http://people.sc.fsu.edu/ burkardt

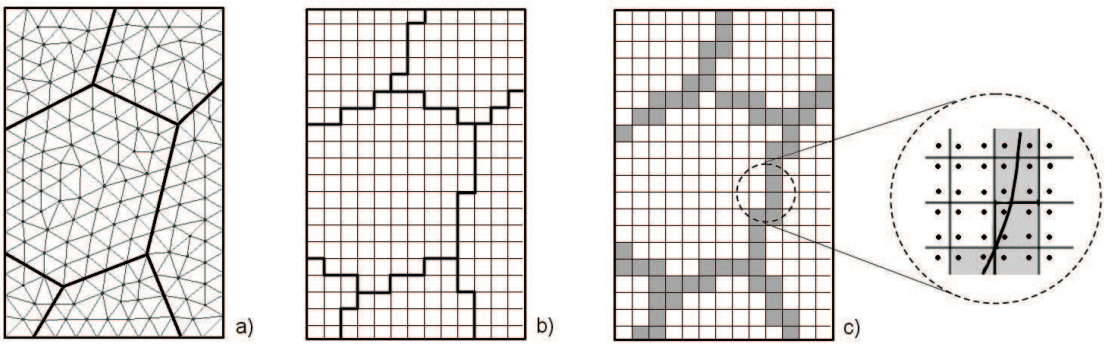

Figure 5: Free mesh (a), regular mesh with "staircase" boundaries (b), and use of multiphase elements (c) in a two-dimensional polycrystal.

of scatter ($V/V_m = 1$ and $A/A_m = 1$) would be obtained only using a tessellation of regular solids as discussed before. Figure 3 shows four aggregates of cubic grains and truncated octahedral grains together with examples of a Voronoi tessellation and of a centroidal Voronoi tessellation. The different grain packing is clear with the regular grain shapes characterized by a repetitive pattern and with the centroidal Voronoi grains more equiaxed and manifesting a more uniform shape distribution than the standard Voronoi. These four types will be used, and the corresponding results compared, in Section 5.

If the generation of Voronoi cells is aimed at the creation of a FE model then the "meshability" is a primary issue. The resulting polyhedra usually have geometric features that would require locally a very fine mesh, but a high level of refinement per grain might imply a computational cost that could reduce the total number of grains in one simulation run. Typical cases of problematic geometric features are shown in Figure 4 and consist in small edges, faces and angles. For example some edges or faces could be a couple of order of magnitude smaller than the average (or desired) element size and this certainly leads to strong element size gradient and possibly to distorted elements. Small angles result in bad element shape metrics, regardless of the size. To improve the mesh quality, some corrections can be applied to the geometry of the grains before the discretization is performed. Figure 4e-f) suggests indeed a possible solution based on the direct removal of the small features obtained by collapsing and merging of edges or vertices. Given a threshold value of acceptance for the edge and face size or for the angle, one could run a check in the whole aggregate and then modify the geometry where needed. It must be mentioned that the suppression of these features could locally eliminate one of the main characteristics of the Voronoi tessellation, i.e. the fact that all the vertices are triple junctions, as more than three edges may converge to one vertex, see Figure 4e). This drawback however should be totally overcome by the mesh quality improvement. The corrective actions in Figure 4e-f) have not been implemented yet by the present authors so the meshes used in Section 5 will unavoidably present some distorted elements.

In the literature other strategies have been proposed and are based on the manipulation of the grain boundaries, more precisely the flatness of faces is altered to allow a quick construction of a regular mesh without any of the problems above, Figure 5b-c). Figure 5a) is the standard approach just discussed and used in this paper, the grain boundaries are flat, every grain is partitioned into finite elements and at the boundaries the mesh is coherent with the neighbors. The second approach, case b), adopts a regular mesh and the boundaries assume a "staircase" pattern that mimics only partially the original flat borders. The evident advantage is that the mesh can be easily created in the whole aggregate; the drawback is the alteration of the grain shapes and the distortion of the boundaries, (Diard et al., 2005). This type of mesh is however suitable when used to replicate real microstructures if the information is in form of a discrete set of voxels or pixels, for example from tomography or EBSD data. A similar idea is applied in case c) of Figure 5, the mesh preserves the same regular pattern but at the grain boundaries "multiphase" elements are adopted. In these special elements part of the integration points belongs to one grain while the remaining part belongs to the neighboring grain, the "staircase" effect is mitigated and the advantages of the regular mesh are preserved.

In all the discussion above, it was tacitly implied that the three-dimensional space to be tessellated was bounded by flat faces, and the simplest case is a unit cube. When the cube is filled with regular solids, some of them have to be trimmed and this is usually done along their symmetry planes. In the case of Voronoi and centroidal Voronoi tessellations, the flat borders are obtained by mirroring the nucleation points. Periodic aggregates can also be constructed as shown in Figure 1: for regular solids this does not require any trimming, for Voronoi tessellations

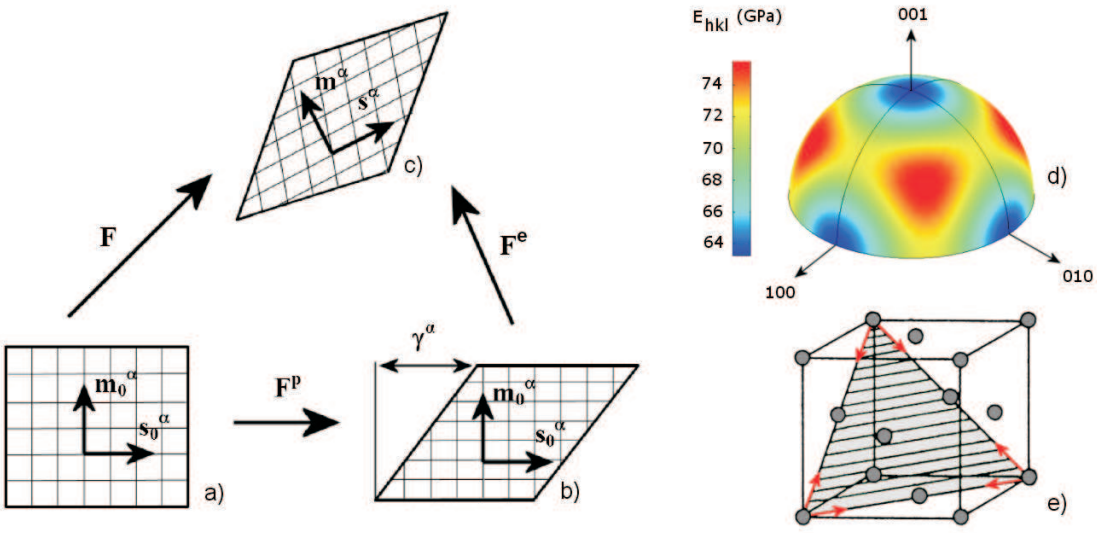

Figure 6: Kinematics of single crystal deformation: (a) reference, (b) intermediate and (c) actual configurations. (d) Directional elastic modulus E_{hkl} plotted on unit hemisphere for aluminum. (e) Schematics of the slip systems $\{111\}$ <110> for an FCC crystal.

the nucleation points have just to be copied and replicated in accordance with the directions where periodicity is desired. In the all simulations presented in Section 5 only flat faces will be used.

4 Crystal constitutive equations

The kinematics of crystal deformation is based on the multiplicative decomposition of the deformation gradient $\boldsymbol{F}$ as in Equation 2 and Figure 6a-c), where $\boldsymbol{F^e}$ is associated with elastic lattice stretching and rigid rotation while $\boldsymbol{F^p}$ is the plastic contribution due to shearing of the slip systems only. $\boldsymbol{F^p}$ represents, in a continuum fashion, the cumulative effect of the dislocation motion in the crystal, therefore it is assumed to leave the crystal lattice undistorted and unrotated. As conventional in metals, the plastic deformation is supposed to occur at constant volume and the incompressibility condition is $det(\boldsymbol{F^p}) = 0$. Although small, elastic volume changes are allowed and $det(\boldsymbol{F^e}) > 0$.

$$\boldsymbol{F} = \boldsymbol{F}^e \boldsymbol{F}^p \tag{2}$$

The intermediate (or relaxed) configuration, Figure 6b, is unique and is obtained from the current configuration, Figure 6c), by elastic unloading and upon returning the lattice to its original orientation. This partition of the deformation gradient is purely conceptual and provides a suitable mathematical framework for the single crystal plasticity theory. Since in this basic formulation the plastic flow takes place uniquely through crystallographic glide, the plastic velocity gradient $\boldsymbol{L^p}$ is completely controlled by the shear rates occurring on the N active slip systems of the crystal; in the intermediate configuration Equation 3 holds:

$$\boldsymbol{L}^p = \sum_{\alpha=1}^{N} \dot{\gamma}^\alpha \boldsymbol{s}_0^\alpha \otimes \boldsymbol{m}_0^\alpha. \tag{3}$$

Each slip system α is defined by the glide direction $\boldsymbol{m_0^\alpha}$ and by the slip plane normal $\boldsymbol{s_0^\alpha}$ given in the reference configuration. These are time-independent orthonormal unit vectors but in the current configuration only the orthogonality is preserved. To define the material behavior both the elastic and plastic deformation must be prescribed at each instant of the analysis. In the elastic behavior of the crystals it is assumed that second-order effects are negligible therefore the constitutive law is linear and anisotropic. The elastic lattice strain $\boldsymbol{E^e}$ is defined in terms of the elastic deformation gradient $\boldsymbol{F^e}$ as:

$$\boldsymbol{E}^e = \frac{1}{2}\Big(\boldsymbol{F}^{eT}\boldsymbol{F}^e - \boldsymbol{I}\Big). \tag{4}$$

The corresponding stress measure, elastic work-conjugate to $\boldsymbol{E^e}$ in the intermediate configuration, is the second Piola-Kirchhoff stress $\boldsymbol{T^e}$. Assuming that the elastic strains are small, which is reasonable since the elastic moduli of metallic materials are usually various orders of magnitude greater than the strengths, the relationship between $\boldsymbol{T^e}$ and $\boldsymbol{E^e}$ is:

$$\boldsymbol{T}^e = \boldsymbol{\mathcal{L}}\boldsymbol{E}^e \tag{5}$$

where $\boldsymbol{\mathcal{L}}$ is the fourth-order elasticity tensor. For crystals with cubic symmetry three independent elastic constants are needed to fully define $\boldsymbol{\mathcal{L}}$: C_{11}, C_{12}, C_{44}. Given the Jacobian determinant $J = det(\boldsymbol{F^e})$, the Cauchy stress tensor $\boldsymbol{\sigma}$ and the elastic stress tensor $\boldsymbol{T^e}$ are related by:

$$\boldsymbol{T}^e = J\boldsymbol{F}^{e-1}\boldsymbol{\sigma}\boldsymbol{F}^{e-T}. \tag{6}$$

The basic physics of slip in crystals is simple, when a slip system activates, it causes the dislocations to move along the slip direction and this induces an accumulation of dislocations, which in turn increases the stress required to promote additional dislocation movement. It is the strain hardening effect: the higher the deformation of the crystal, the more work is required to induce further straining. The equations that rule these concepts must be specified locally for every slip system. Two quantities are involved in the definition of the slip rates: the resolved shear stress τ^α on the α-th slip system (the stress component that acts in the direction of slip), and the slip system deformation resistance g^α. The material model adopted here is rate-dependent inasmuch as the slip rates $\dot{\gamma^\alpha}$ are uniquely determined in terms of the described deformation or stress rates. In rate-dependent models there is not explicit yielding and all slip systems are inherently active, plastic shearing on the α-th slip system occurs as soon as the resolved shear stress τ^α is nonzero. The flow rule is a kinetic relation with a general form $\dot{\gamma}^\alpha = f(\tau^\alpha, g^\alpha)$. A fairly common power law relationship, (Hutchinson, 1976; Pan and Rice, 1983), is:

$$\dot{\gamma}^\alpha = \dot{\gamma}_0 \left| \frac{\tau^\alpha}{g^\alpha} \right|^{1/m} \mathrm{sgn}(\tau^\alpha) \tag{7}$$

which is suited for a limited range of strain rates about a constant reference value, $\dot{\gamma}_0$. The parameter m is the material rate sensitivity and the rate-independent limit is reached when $m \to 0$. All the slip systems are considered to have the same initial resistance g_0, however, since the various slip systems affects the others, the evolution equation (hardening law) of the strength g^α is:

$$\dot{g}^\alpha = \sum_{\beta=1}^{N} h^{\alpha\beta} |\dot{\gamma}^\beta|. \tag{8}$$

The hardening matrix $h^{\alpha\beta}$ represents the slip hardening rates, every coefficient accounts for the effect of β-*th* slip system on the α-*th*. The expression used here is:

$$h^{\alpha\beta} = \left[q + (1-q)\delta^{\alpha\beta} \right] h^\beta \tag{9}$$

where q is a latent-hardening parameter and h^β is the self-hardening rate:

$$h^\beta = h_0 \left| 1 - \frac{g^\beta}{g^s} \right|^a. \tag{10}$$

In the FCC crystals considered in this work, the hardening parameters a, g_s, g_0 and h_0 are assumed to be identical for all the slip systems. The resolved shear stress on the α-th slip system is finally calculated through the following expression:

$$\tau^\alpha = J\boldsymbol{\sigma}\cdot(\boldsymbol{s}^\alpha \otimes \boldsymbol{m}^\alpha). \tag{11}$$

The constitutive equations above have been implemented as a material model in the commercial finite element program ABAQUS/Standard through a user material subroutine *UMAT*. The numerical integration of the equations follows essentially the procedures proposed in (Kalidindi et al., 1992) and (Anand, 2004).

Table 1: Suite of grain aggregates used in the FE simulations.

orientations	polycrystalline mesh			
set 1	CUB1	TO1	CVT1	VOR1
set 2	CUB2	TO2	CVT2	VOR2
set 3	CUB3	TO3	CVT3	VOR3

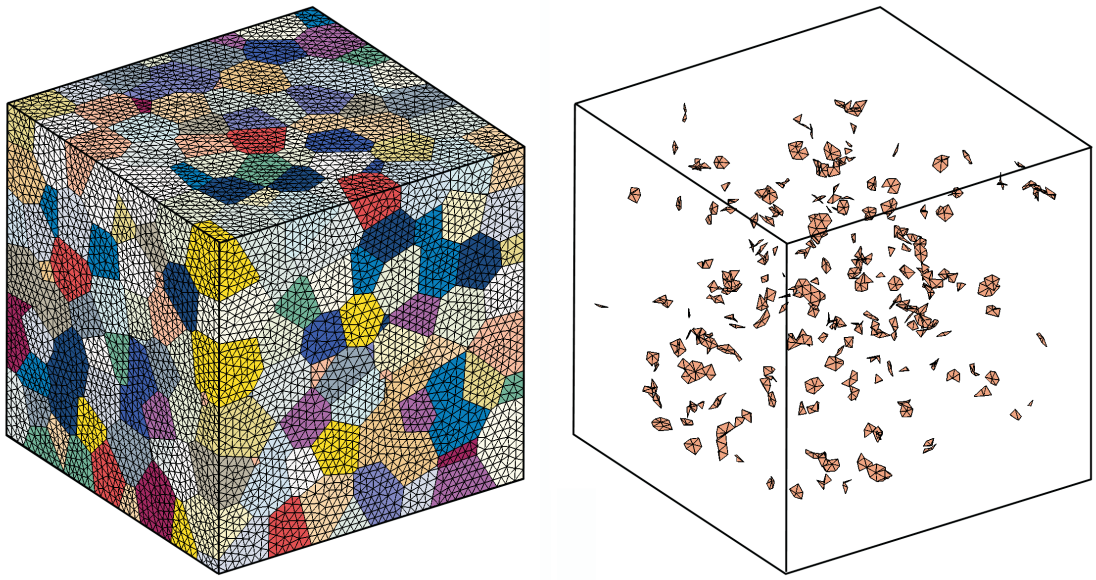

Figure 7: (a) Mesh on the surface of polycrystal *CVT1* and (b) distorted elements in the interior.

5 FE simulations

In the series of FE simulations carried out, three set of 559 grain orientations and four type of grain arrangements were considered. The polycrystals were confined in unit cubes with flat faces to ease the application of the boundary conditions. Each set of orientations was obtained by randomly sampling a uniform orientation distribution therefore, at the beginning of the simulation, each polycrystal had no preferred crystallographic texture. Referring to Section 3, two grain arrangements were constructed from regular grain shapes, cube (*CUB*) and truncated octahedron (*TO*). The other two types were derived from tessellation of space using irregular convex solids. One type was the conventional Voronoi tessellation (*VOR*) based on randomly distributed nucleation points. Three set of different nucleation points were created giving therefore three distinct grain aggregates. These aggregates were then transformed into corresponding centroidal Voronoi tessellations (*CVT*) through the minimization process outlined in Section 3, therefore other three polycrystals were assembled. The complete set of virtual polycrystals analyzed is summarized in Table 1. Figure 3 shows examples of grains internal to the polycrystals.

A high number of grains is required to have a good statistical description of the microstructure of the material and to provide a macroscopic response in agreement with the experimental observations. Additionally each crystal should be resolved in several finite elements to better catch the local heterogeneities at the crystal scale, (Zhao et al., 2007). Both requirements, together with the high non-linearity of the constitutive equations, determine the computational cost of the single simulation. The fine discretization of the crystals was judged essential in this study, so the number of elements per grain in the cubic grains was 648, in truncated octahedra was 912 (this refers to the complete solids, excluding the trimmed ones at the polycrystal surfaces). For families *VOR* and *CVT* the average number of elements per grain was about 685. The number of grains in each aggregate was set equal to 559 for aggregates *TO*, *VOR* and *CVT* while it was equal to 512 for type *CUB*. The latter comes simply from the partition

Table 2: Material parameters of the aluminum alloy.

C_{11} (GPa)	C_{12} (GPa)	C_{44} (GPa)	m	$\dot{\gamma}_0$ (s^{-1})	h_0 (MPa)	g_0 (MPa)	g_s (MPa)	a	q
107.3	60.9	28.3	0.012	0.001	700	75	170	2.2	1.4

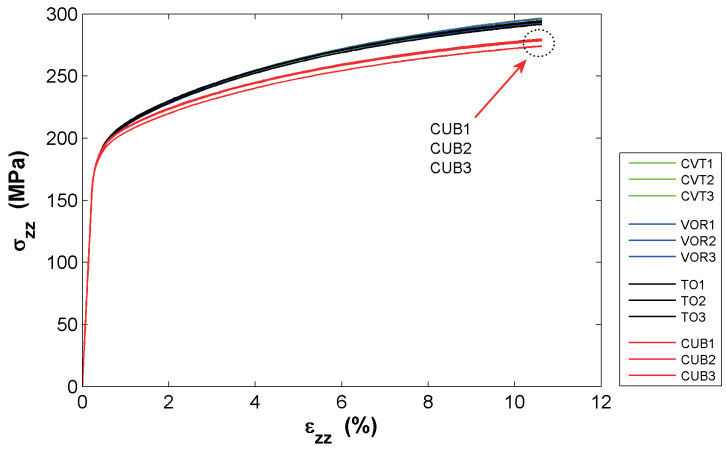

Figure 8: Macroscopic (engineering) stress-strain curves obtained from the twelve polycrystals.

of each edge in 8 cubes. Summing up all the grains of the twelve aggregates in Table 1 the total number is 6567. The *CUB* polycrystals had 331776 elements, the *TO* types had 393984, the other meshes consisted of about 380000 elements each. Four-noded tetrahedral (linear) elements were used. The *CUB* and *TO* polycrystalline meshes did not suffer from any of the problems in Figure 4, on the other hand *VOR* and *CVT* presented several distorted elements. The number of highly distorted elements was estimated to be about $1500 \div 2000$ which is $0.4 \div 0.5\%$ of the total number of finite elements. Some more thousands elements had poor shape metrics parameters but, unfortunately, this is quite the rule with such complex geometries. An example of mesh is given on the left of Figure 7, on the right the highly distorted elements inside the polycrystal are isolated. In all the data analysis presented in Section 6 the distorted elements were discarded to avoid introducing spurious effects on the validity of the results.

At the beginning of the simulations the same lattice orientation was assigned to all the elements in each grain. Upon deformation the orientation of the elements is however expected to evolve differently thus creating misorientation fields over the whole polycrystals. For all the entries in the matrix of Table 1, the assignment of the orientations to the grains was random for type *CUB*, *TO* and *VOR*. For type *CVT* the grains had the same orientations as the original Voronoi cells before the minimization process. Symmetry boundary conditions were set to three faces of the polycrystals, a uniform displacement along the loading direction (z) was applied to a face parallel to plane $x-y$, and the remaining two surfaces were free to deform. The displacement was such that the strain rate resulted in a constant value $\dot{\varepsilon} = 0.001\ s^{-1}$. The maximum engineering strain reached was 10% which represents a condition with a fully developed plasticity. The reference material employed here is a AlSi7Mg alloy with macroscopic mechanical properties as follow: yield stress = 215 MPa, ultimate stress = 315 MPa and fracture strain about 15%. The material parameters of the aluminum alloy were obtained by matching the macroscopic stress-strain curves and are reported in Table 2. The elastic constants are from (Hosford, 1993) and the latent hardening parameter q in Equation 9 is set equal to 1.4 which holds for non-coplanar slip systems in FCC crystals, (Anand, 2004).

6 Results and discussion

The macroscopic stress-strain curves obtained from the FE simulations are plotted in Figure 8. The curves are fairly similar for all the polycrystals except type *CUB* which exhibit a slightly softer behavior. At the maximum strain ($\varepsilon = 10\%$) the average difference in stress is about 15 MPa with respect to *TO*, *VOR* and *CVT*. The three set of orientations show also some discrepancies but this is probably due to the relatively low number of grains in the aggregates, especially in type *CUB*. However the number of grains alone cannot justify the softer response of the polycrystals *CUB* so the reasons have to be found in grain shape which evidently influences the way the deformation is distributed in the aggregate. This will become more evident in the following.

The crystal-scale behavior is now considered, in particular the plastic strain and the intra-granular misorientations. They are caused by the local slip system activity and by the change in orientation that develop upon deformation.

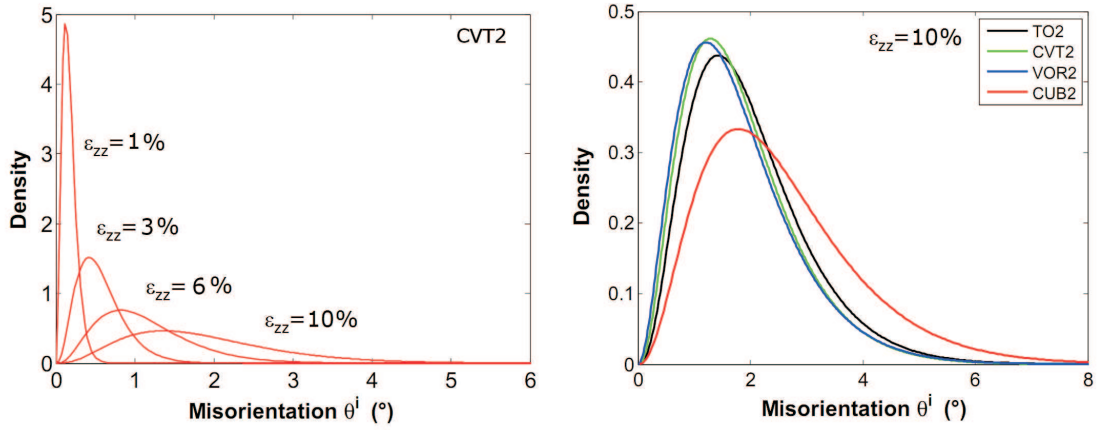

Figure 9: (a) Distributions of the misorientations θ^i in aggregate *CVT2*. (b) Comparison of the distributions at ε_{zz}=10% for aggregates with set of orientations 2.

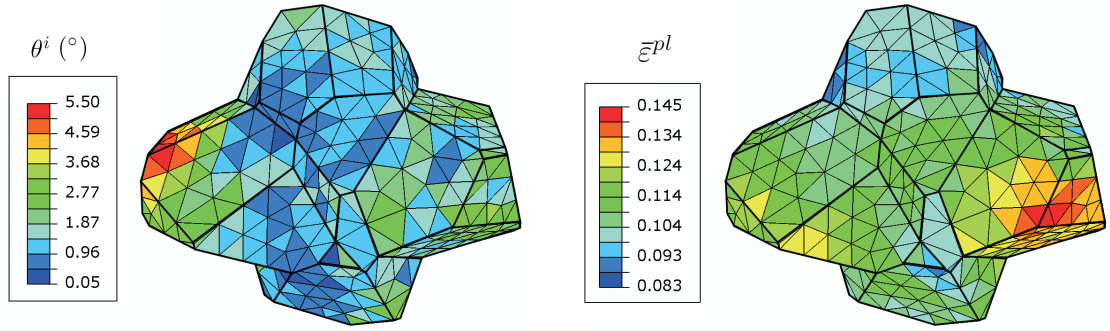

Figure 10: (a) Misorientations and (b) equivalent plastic strain in a cluster of grains in the bulk of aggregate *CVT1*, ε_{zz}=10%.

Two scalar variables are used here to quantify them, the first is the conventional equivalent plastic strain:

$$\bar{\varepsilon}^{pl} = \int_0^t \sqrt{\frac{2}{3}\boldsymbol{D}^p : \boldsymbol{D}^p}\, dt \tag{12}$$

where $\boldsymbol{D}^p$ is the symmetric part of the plastic velocity gradient $\boldsymbol{L}^p$ and t is the current time of the analysis. This gives an average measure of the accumulated slip systems activity in the finite elements, and since the loading is monotonic (without neither changes in path nor unloadings) $\bar{\varepsilon}^{pl}$ always increases with the macroscopic strain. The second variable is related to the re-orientation field that takes place within the crystals. More specifically the focus here is on the differences between the local orientation of the elements constituting a grain and the average orientation of the whole grain. In general, given a set of *n* lattice orientations, known at specific points in a deformed grain, it is possible to define an average orientation θ^{avg}, (Barton and Dawson, 2001). These points can be locations in a physical sample where orientations are measured through diffraction techniques, or can be points in the mesh of virtual polycrystals. The latter is the case here as for each element in the mesh the orientation is known at several instant along the loading history. The misorientation angle of element i with respect to θ^{avg} is labeled θ^i and it is a positive value. Considering all the elements in the mesh[2], a gamma distribution is found to well estimate the probability density function of the misorientations θ^i. Referring for example to aggregate *CVT2*, Figure 9a) shows the evolution of the fitted distributions for some macroscopic strain levels. At ε_{zz}=1% the misorientations $\theta^i$are still low and the scatter is very weak, but as the deformation fully enters in the plastic regime the mean value increases and, above all, the distributions widen. The other aggregates show the same trends and the comparison at ε_{zz}=10% for the set of orientation 2 is reported in Figure 9b) (very similar curves are obtained for sets 1 and 3). Here it is observed that type *CUB* differentiates from the others because of higher misorientations.

[2]The distorted elements are excluded from all the data analysis presented in this Section.

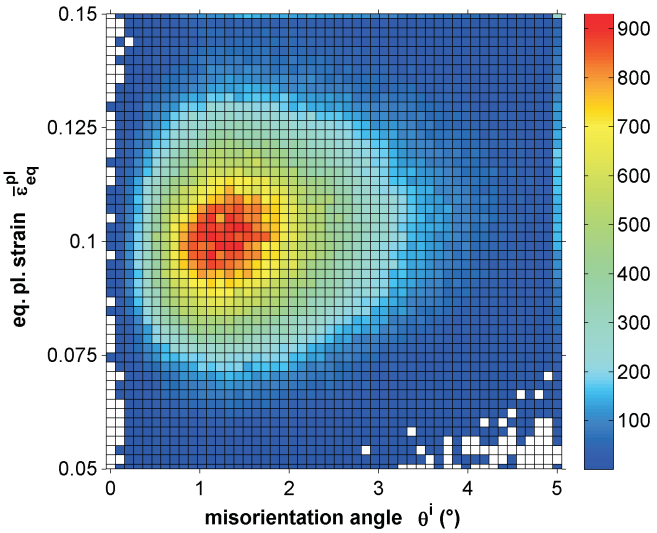

Figure 11: Frequency histogram θ^i- $\bar{\varepsilon}^{pl}$ for the elements in aggregate *CVT1* at ε_{zz}=10%.

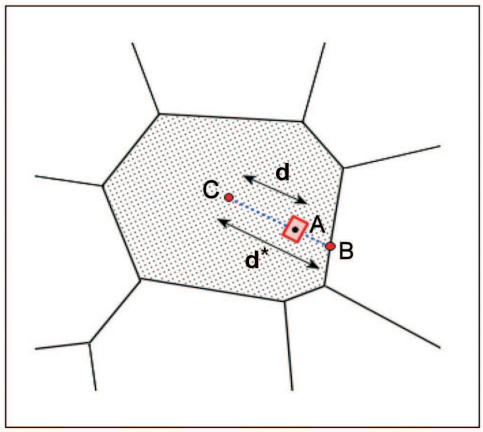

Figure 12: Two-dimensional representation of the distances d (between the grain centroid C and the element centroid A) and d^* (between the grain centroid C and the grain boundary B).

The equivalent plastic strain $\bar{\varepsilon}^{pl}$ shows a very heterogeneous pattern in the polycrystals and it is known to be caused by the different attitude to crystallographic slip of the constituent grains (due to the orientation with respect to the load direction) and by the constraining effect of the neighboring grains that forces each crystal to deform in a compatible way. Locally the role of the grain boundary is important since they separate areas with contrasting orientation and therefore different behavior. The regions close to the grain boundaries are expected to act differently from the grain center, at least till large deformation involves massively the grain and phenomena such as grain splitting or banding strongly change the local properties or the orientation. It is stimulating to investigate if there is a correlation between the local accumulated plastic strain and the misorientation. An example is given in Figure 10 where four grains, isolated from the bulk of aggregate *CVT1*, are visualized with contour maps of $\bar{\varepsilon}^{pl}$ and θ^i at ε_{zz}=10%. Several elements on the grain surfaces have quite low misorientation indicating that their orientation is not far from the respective grain average θ^{avg}, but some elements show however high values. Similar considerations can be drawn looking at the equivalent plastic strain: the field is not homogeneous and peaks are found on the grain surfaces, i.e. the grain boundaries. From this only extract one might conclude that an element-by-element correlation between θ^i and $\bar{\varepsilon}^{pl}$ does not exist. The proof comes from Figure 11 which is a frequency histogram (in form of a 50x50 matrix) that relates the misorientation and the equivalent plastic strain of all the elements in aggregate *CVT1* at the maximum strain level (10%). The number of finite elements in each cell determines the color. The iso-values lines that can be pictured are quite circular and therefore a direct relationship between θ^i and $\bar{\varepsilon}^{pl}$ could be reasonably excluded, at least for the range of macroscopic strain investigated here. Once again the same pattern is found analyzing the other eleven polycrystals in Table 1.

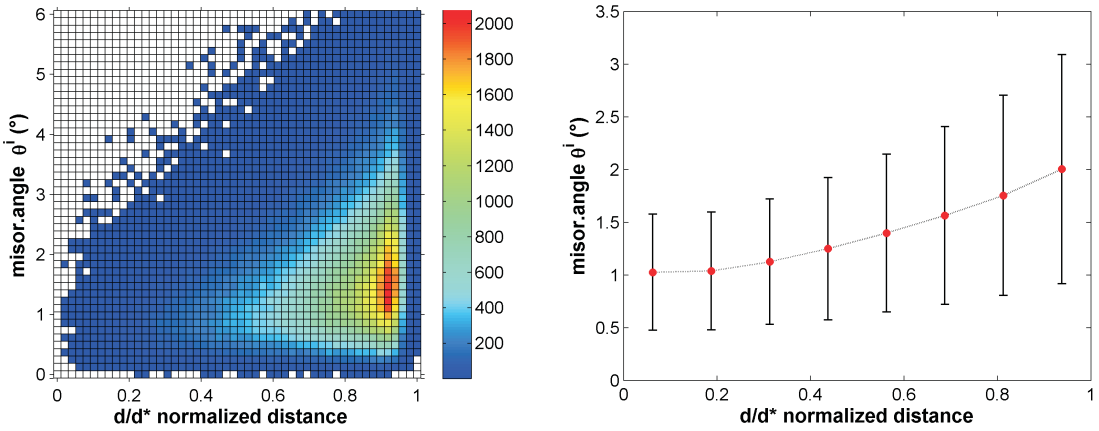

Figure 13: Frequency histogram matrix θ^i - d/d^* of the elements in polycrystal *VOR3* at ε_{zz}=10% (left). Equivalent representation after reducing the data in 8 bins and calculating the mean value and the standard deviation (right).

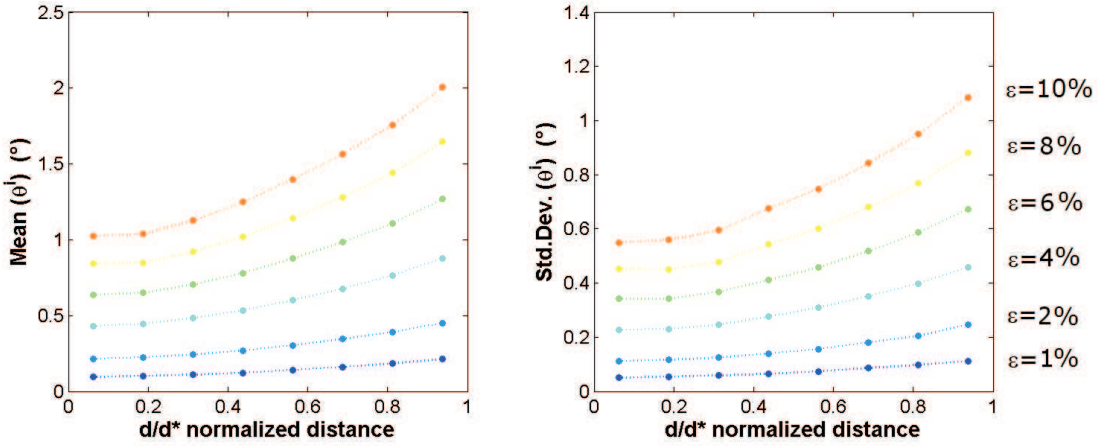

Figure 14: Mean value and standard deviation of θ^i in the 8 bins of d/d^* at different macroscopic strain levels. The plots refer to aggregate *VOR3*.

From the experimental point of view, intra-grain misorientation are of interest because they can be used to understand and quantify the storage of dislocations and the inhomogeneous straining occurring within grains. Often in fact the experimental evaluation of the slip system activity can be difficult, instead, the underlying activity can be estimated in terms of the local lattice re-orientations. The results obtained from the simulations here suggest that this strict correlation might be questionable.

The attention is now turned to the intra-grain behavior and more specifically to the spatial variation of the two chosen variables inside the crystals. The influence of the grain boundaries is studied in an average way introducing the parameter "position" inside the crystal. Referring to the two-dimensional case of Figure 12, let C be the centroid of the grain and A be the centroid of one element constituting the grain. In linear tetrahedral elements the centroid coincides with the only integration point, where all the field variables are usually available as output. A straight segment stemming from C and passing trough A is constructed and extended until it intercepts a grain boundary in a point B. Now if distance $C - A$ is called d and the distance $C - B$ is labeled d^* then d/d^* becomes the normalized location of the element with respect to the grain center and the impinged grain boundary. Note that due to the convexity of all the grains there is one and only one possible solution to the calculation of d^*. This calculation necessitates the mathematical representations of the grains in terms of vertices, edges and faces. The idea is to compute the parameter d/d^* for all the elements in each grain in the virtual aggregates and to investigate the spatial variation of some quantities within the grains. Figure 13a) shows the frequency matrix of the misorientation angle θ^i and the normalized distance d/d^* for polycrystal *VOR3* at the macroscopic strain of 10%. To better emphasize the most populated region of the graph the upper bound of $\theta^i$is set to 6°. The number of elements obviously augments as d/d^* moves from 0 to 1, but superimposed there is also an increment both in the average θ^i and in the range of misorientations. These trends appear more clearly if the normalized

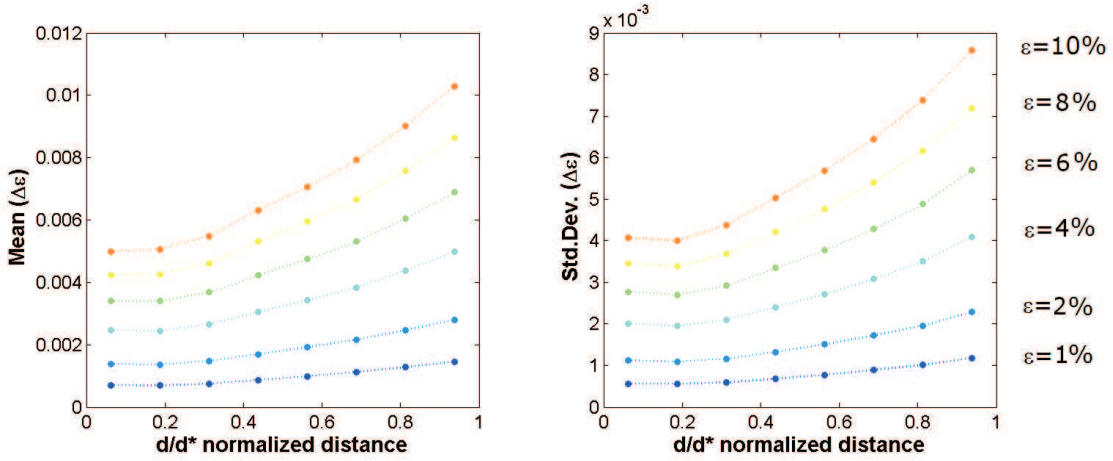

Figure 15: Mean value and standard deviation of $\Delta\varepsilon$ in the 8 bins of d/d^* at different macroscopic strain levels. The plots refer to aggregate *VOR3*.

distance d/d^* is binned in a reduced number of intervals, say 8, and the mean and standard deviation of the misorientation of the elements inside each bin is calculated. The results of such procedure are reported in Figure 13b). The misorientation θ^i becomes progressively higher as the location of the element inside the grain moves from the centroid towards the closest grain boundary. The trend has a parabolic nature and the mean value of θ^i inside the first bin (position close to the centroid) is about 1° whereas in the last bin (position close to the grain boundary) is about 2°. The error bars indicate that also the deviation from the mean value is more pronounced towards the boundaries with a maximum value of 1.1° in the last bin which represents a considerable fraction of the corresponding mean value. The evolution of the intra-granular misorientation field as a function of the macroscopic straining ε_{zz} is shown in Figure 14 for the same polycrystal *VOR3*. The mean value and the standard deviation are separated in two plots and are reported for six different levels of ε_{zz}. As expected the higher the macroscopic strain the higher the misorientations, but also the scatter increases with ε_{zz}.

The same analysis scheme can be applied to other field variables, for example the accumulated plastic strain $\bar{\varepsilon}^{pl}$, to ascertain the regions inside the grains more or less prone to deform. To emphasize the differences between the grain average and the quantities at each element a parameter $\Delta\varepsilon$ defined as in Equation 13 is introduced:

$$\Delta\varepsilon = |\bar{\varepsilon}^{pl} - \bar{\varepsilon}^{pl}_{avg}|. \tag{13}$$

$\Delta\varepsilon$ represents the difference between the elemental equivalent plastic strain $\bar{\varepsilon}^{pl}$ and the grain average value $\bar{\varepsilon}^{pl}_{avg}$, the absolute value is used to capture the relative difference disregarding the sign, in fact the slip system activity at the center of the grain is expected to have dissimilarities compared to the regions close to the boundaries. This was already observed in Figure 10b) and in particular in the crystal on the right, here the grain average is about 0.119 and many visible elements have $\bar{\varepsilon}^{pl}$ close to this value but both the maximum (0.145) and the minimum (0.094) are on the faces that act as grain boundaries. Not all the grains however exhibit such a strong mismatch between the maximum and the minimum values of $\bar{\varepsilon}^{pl}$. Considering now all the grains in one of the aggregates, for instance *VOR3*, the computed values of the parameter $\Delta\varepsilon$ in each bin along the normalized distance d/d^* is given in Figure 15. Here once more it is confirmed that towards the periphery of the crystals there is a higher discrepancy with respect to the grain average. Given the definition of $\Delta\varepsilon$ in Equation 13, this mismatch comes either from elements that go trough an extensive deformation or from elements where slip is somehow limited. Both the mean curves and the standard deviation curves show a progressive growth and they peak near the grain boundaries. The evolution of $\Delta\varepsilon$ with the macroscopic strain coincides with the trend of the misorientation θ^i, in fact the mean and the deviations values of $\Delta\varepsilon$ increase parabolically with ε_{zz}. This means that the plastic strain heterogeneity, as described by $\Delta\varepsilon$, is in average stronger as the elasto-plastic transition is passed and keeps growing with the application of the strain. Moving from the grain boundary (last bin) towards the grain center (first bin) both the mean value and the standard deviation of $\Delta\varepsilon$ almost halves for basically all the strain levels considered here. At ε_{zz}=10% the mean difference between the first bin and the last bin is about 0.05 which represents the 50% of the macroscopic total strain. Another remark comes from the relative distance of the curves which slightly reduces as the deformation increases (at least in the range of macroscopic strain considered here), this means that the rate at which the plastic strain heterogeneity changes with respect to the grain average lessens with the macroscopic strain. The standard deviations in Figure 15b) exhibit pretty the same features. It should be mentioned that in both

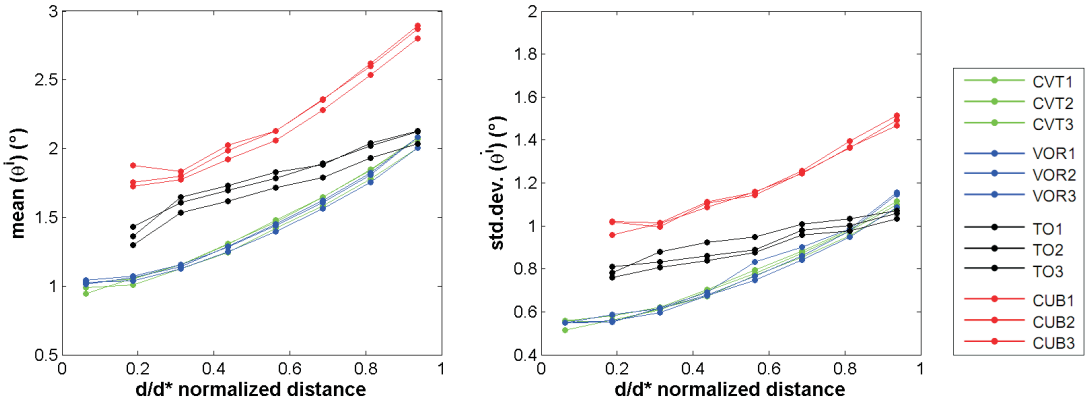

Figure 16: Mean values and standard deviations of θ^i in the 8 bins along d/d^*. Comparison between all the polycrystalline aggregates.

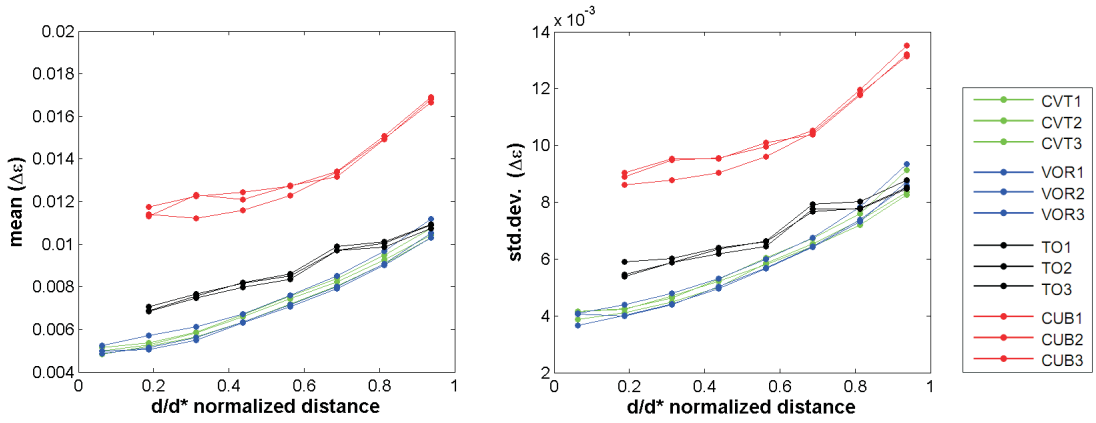

Figure 17: Mean values and standard deviations of $\Delta\varepsilon$ in the 8 bins along d/d^*. Comparison between all the polycrystalline aggregates.

Figure 15 and 14 the bins contain a different number of elements (for example: some hundreds in the first bin, some thousands in the second bin and more than 10e5 in the eighth bin) so the calculated values have not the same statistical basis. Nonetheless the trends are quite consistent therefore even the data from the less populated bin are deemed to be acceptable.

The procedure was then applied to all the other eleven polycrystals and the comparison is given in Figure 16 for the misorientations θ^i and in Figure 17 for the parameter $\Delta\varepsilon$. Because of the regularity and topology of the mesh of each grain (with multiple symmetries for the cubes and for the truncated octahedra), the first bin is empty for types *CUB* and *TO* as no elements have the centroid close enough to the grain center. The first comment that can be done deals with the set of orientations: the number of grains adopted is quite sufficient to grant a comparable response because, for each type of tessellation, the differences between the curves are small. The second comment has to do with the comparison between the types of grain aggregates, in fact it is found that family *VOR* and family *CVT* show very similar behavior both for θ^i and for $\Delta\varepsilon$. These curves represent also the lower bounds for all the cases studied here. On the other hand, the aggregates with cubic grains (family *CUB*) act as the upper bounds and the values are about twice the values of *CVT* and *VOR*. Type *TO* is intermediate but tends to converge to the lower bound for d/d^* approaching to 1. Curves *TO* do not follow so well the parabolic trend discussed before but this is blamed again to the mesh in fact, even if there are many elements in each complete grain (648), because of the regularity there is a small set of distances d/d^* and they do not coincide exactly with the number of bins chosen here. The use of quadratic tetrahedral elements would, in general, improve the quality of the results and, due to the higher number of integration points, would also increment the number of points A (as defined in Figure 12) to be selected for the bins. Obviously the computational cost of such FE simulations would increase quite considerably. From all the results presented here, really noticeable differences between *CVT* and *VOR* were not found. Even if

CVT has a more uniform grain distribution, still the complexity of the crystal shapes and of the network of grain boundaries determines a behavior comparable to type *VOR*. Cubic grains always gave discrepant results from the other tessellations. TO aggregates probably represent a good compromise between complexity of the grain shape and the quality of the mesh; most of the results were aligned with *CVT* and *VOR*.

Although the grains at the free surface may behave differently from the grains in the bulk, this aspect is neglected in this work and all the grains in the polycrystals were considered in the data analysis. No grains were excluded to maintain a sufficiently high number of grains for good statistics. A finer discretization of the mesh in each grain could also better resolve the plastic strain and misorientation fields. The specific role of the triple junctions, present in all the twelve aggregates, cannot emerge from the averaging procedure introduced here. The study of the triple, or multiple, junctions is certainly complicated by the contribution of three, or more, grains; stress fluctuations and stress singularities were in fact found from crystal plasticity simulations in (Kanjarla et al., 2009). Another interesting extension of the work would include the analysis of the local fields across the grain boundaries where stress and strain heterogeneities are induced by the compatibility necessary to accommodate the shape and orientation changes in neighbor grains. It is emphasized again that the model employed does neither explicitly consider the dislocations (or the dislocation density) nor incorporates strain-gradient or non-local effects. Relevant phenomena such as slip transmission, dislocation generation, annihilation, absorption or reflection at the grain boundaries are therefore not accounted for. It is however expected that their implementation could enrich the quality of the results and possibly provide different scenarios.

7 Conclusions

In this work a review of the most common techniques for the construction of polycrystalline aggregated to be employed in FE simulations was presented. Advantages and drawbacks of the use of regular solids or irregular tessellations were outlined. The quality of the mesh is definitively better for regular solids but the Voronoi tessellation provides aggregates more close to reality. A modified version, called centroidal Voronoi tessellation, was proposed as an alternative to the standard Voronoi procedure. This tessellation gives a more uniform distribution of grains both in size and in shape. From the simulations of the twelve aggregates of the aluminum alloy several topics were analyzed. The cubic grain shape provides a slightly softer macroscopic stress-strain curve compared to the other polycrystals. The misorientation distribution in aggregate types *TO*, *VOR* and *CVT* was found to be very similar, type *CUB* showed a higher level of misorientations. On an element-by-element basis a correlation between the plastic strain and the misorientation was not evident. The role of the grain boundaries as source of heterogeneities was illustrated trough an original analysis of the intra-granular plastic strain and misorientation fields. Close to the boundaries higher differences (and wider scatter) were found with respect to the grain center and the values are a function of the macroscopic strain level.

References

Anand, L.: Single-crystal elasto-viscoplasticity: application to texture evolution in polycrystalline metals at large strains. *Com. Met. Appl. Mech. Engrg.*, 193, (2004), 5359 – 5383.

Barton, N.; Dawson, P. R.: A methodology for determining average lattice orientation and its application to the characterization of grain substructure. *Metall. Mater. Trans. A*, 32, (2001), 1967 – 1975.

Dawson, P. R.; Boyce, D. E.; MacEwen, S.; Rogge, R.: On the influence of crystal elastic moduli on computed lattice strains in aa-5182 following plastic straining. *Mater. Sci. Eng. A*, 313, (2001), 123 – 144.

Diard, O.; Leclercq, S.; Rousselier, G.; Cailletaud, G.: Evaluation of finite element based analysis of 3d multicrystalline aggregates plasticity application to the crystal plasticity model identification and the study of stress and strain fields near grain boundaries. *Int. J. Plasticity*, 21, (2005), 691 – 722.

Du, Q.; Faber, V.; Gunzburger, M.: Centroidal voronoi tessellations: applications and algorithms. *SIAM Review*, 41, (1999), 637 – 676.

Erieau, P.; Rey, C.: Modeling of deformation and rotation bands and of deformation induced grain boundaries in if steel aggregate during large plane strain compression. *Scripta Mater.*, 20, (2004), 1763 – 1788.

Fu, X.; Poulsen, H. F.; Schmidt, S.; Nielsen, S. F.; Lauridsen, E. M.; Jensen, D. J.: Non-destructive mapping of grains in three dimensions. *Scripta Mater.*, 49, (2003), 1093 – 1096.

Héripré, E.; Dexet, M.; Crépin, J.; Gélébart, L.; Roos, A.; Bornert, M.; Caldemaison, D.: Coupling between experimental measurements and polycrystal finite element calculations for micromechanical study of metallic materials. *Int. J. Plasticity*, 23, (2007), 1512 – 1539.

Hosford, W. F.: *The Mechanics of Crystals and Textured Polycrystals*. Oxford University Press, New York (1993).

Hughes, D. A.; Hansen, N.: High angle boundaries formed by grain subdivision mechanisms. *Acta Metall.*, 45, (1997), 3871 – 3886.

Hutchinson, J. W.: Bounds and self-consistent estimates for creep of polycrystalline materials. *Proc. Roy. Soc. Lond. A*, 348, (1976), 101 – 127.

Kalidindi, S. R.; Bhattacharyya, A.; Doherty, R. D.: Detailed analyses of grain-scale plastic deformation in columnar polycrystalline aluminium using orientation image mapping and crystal plasticit ymodels. *Proc. R. Soc. Lond. A*, 460, (2004), 1935 – 1956.

Kalidindi, S. R.; Bronkhorst, C. A.; Anand, L.: Crystallographic texture evolution in bulk deformation processing of fcc metals. *Mech. Phys. Solids*, 40, 3, (1992), 537 – 569.

Kamaya, M.; Wilkinson, A. J.; Titchmarsh, J. M.: Measurement of plastic strain of polycrystalline material by electron backscatter diffraction. *Nuc. Eng. Design*, 235, (2005), 713 – 725.

Kanjarla, A. K.; Van Houtte, P.; Delannay, L.: Assessment of plastic heterogeneity in grain interaction models using crystal plasticity finite element method. *Int. J. Plasticity*, doi:10.1016/j.ijplas.2009.05.005.

Kuhlmann-Wilsdorf, D.; Hansen, N.: Geometrically necessary, incidental and subgrain boundaries. *Scr. Metall. Mater.*, 25, (1991), 1557 – 1562.

Pan, J.; Rice, J. R.: Rate sensitivity of plastic flow and implications for yield-surface vertices. *Int. J. Solids Struct.*, 19, (1983), 973 – 987.

Raabe, D.; Sachtleber, M.; Weiland, H.; Scheele, G.; Zhao, Z.: Grain-scale micromechanics of polycrystal surfaces during plastic straining. *Acta Mater.*, 51, (2003), 1539 – 1560.

Sachtleber, M.; Zhao, Z.; Raabe, D.: Experimental investigation of plastic grain interaction. *Mater. Sci. Eng. A*, 336, (2002), 81 – 87.

Sarma, G. B.; Dawson, P. R.: Texture predictions using a polycrystal plasticity model incorporating neighbor interactions. *Int. J. Plasticity*, 12, (1996), 1023 – 1054.

Sumigawa, T.; Kitamura, T.; Ohishi, K.: Slip behaviour near a grain boundary in high-cycle fatigue of polycrystal copper. *Fatigue Fract. Engng. Mater. Struct.*, 27, (2004), 495 – 503.

Tatschl, A.; Kolednik, O.: A new tool for the experimental characterization of micro-plasticity. *Mater. Sci. Eng. A*, 339, (2003), 265 – 280.

Thorning, C.; Somers, M. A. J.; Wert, J. A.: Grain interaction effects in polycrystalline cu. *Mater. Sci. Eng. A*, 397, (2005), 215 – 228.

Zhang, K. S.; Wu, M. S.; Feng, R.: Simulation of microplasticity-induced deformation in uniaxially strained ceramics by 3-d voronoi polycrystal modelling. *Int. J. Plasticity*, 21, (2005), 801 – 834.

Zhao, Z.; Kuchnicki, S.; Radovitzky, R.; Cuitiño, A.: Influence of in-grain mesh resolution on the prediction of deformation textures in fcc polycrystals by crystal plasticity fem. *Acta Mater.*, 55, (2007), 2361 – 2373.

Address: Dr. Tito Marin and Prof. Gianni Nicoletto, Department of Industrial Engineering, University of Parma, I-43100 Parma, Italy.
email: marin@ied.eng.unipr.it; gianni.nicoletto@unipr.it